Article

Reverse-Bias Defect Creation in Cu(In,Ga)Se$_2$ Solar Cells and Impact of Encapsulation

Timon Sebastian Vaas [1,2,]*, Bart Elger Pieters [1], Andreas Gerber [1] and Uwe Rau [1,2]

1   IEK5-Photovoltaik, Forschungszentrum Jülich, 52425 Jülich, Germany
2   Jülich Aachen Research Alliance (JARA-Energy) and Faculty of Electrical Engineering and
    Information Technology, RWTH Aachen University, Schinkelstr. 2, 52062 Aachen, Germany
*   Correspondence: t.vaas@fz-juelich.de

Abstract: Reverse breakdown in Cu(In,Ga)Se$_2$ (CIGS) solar cells can lead to defect creation and performance degradation. We present pulsed reverse-bias experiments, where we stress CIGS solar cells with a short reverse voltage pulse of ten milliseconds and detect the electrical and thermal response of the cell. This way, we limit the duration of the reverse stress, allowing us to study the initial stages of reverse-bias defect creation in CIGS solar cells and modules. Our results show that permanent damage can develop very fast in under milliseconds. Furthermore, we find the location of defect creation as well as the susceptibility to defect creation under reverse bias depends strongly on whether the cell is encapsulated or not, where encapsulated cells are generally more robust against reverse bias.

1. Introduction

Partial shading of thin-film photovoltaic (PV) modules can lead to reverse-bias conditions in individual cells and can further result in hotspots and performance degradation. This is especially problematic in integrated PV applications, where partial shading is not always avoidable during operation. The uneven irradiation on the PV module causes different photocurrents in the individual cells, leading to an overall module current that exceeds the photocurrent of these cells. Depending on the difference between the overall module current and the photocurrent of individual cells, the working point of one or more individual cells can be shifted to a reverse-bias condition. Hence, partial shading can cause power dissipation in individual cells. The series connection of many cells in a module means the module is able to provide a voltage well above the junction breakdown voltage of a single cell. Thus, partial shading may lead to junction breakdown in individual, shaded cells.

A junction breakdown in individual cells leads to a decrease in power output due to the dissipation of heat in the reverse-biased cells, but it does not necessarily cause permanent damage. However, under partial shading and reverse bias, thin-film PV technologies are susceptible to the creation of local defects causing a permanent performance degradation. In hydrogenated amorphous silicon (*a*-Si:H) solar cells, reverse stress can lead to the creation of hotspots and permanent shunt-like defects [1].Johnston et al. found similar effects of reverse stress on cadmium telluride (CdTe) solar cells [2].

Bakker et al. provide a detailed literature review of the current status of research on partial shading and reverse bias damage in Cu(In,Ga)Se$_2$ (CIGS) solar cells and modules [3], respectively. In general, partial shading of CIGS modules is known to lead to accelerated degradation caused by the creation of local defects [4–8] attributed to the creation of local hotspots under reverse-bias conditions [2,9–13]. The defects appear as local shunt paths in electroluminescence (EL) and dark lock-in thermography (DLIT) images

leading to a performance loss due to a reduced fill factor. Furthermore, reverse stress can lead to the propagation of hotspots through the cell and therefore to the creation of "wormlike" damages first described by Westin et al. [9]. In addition, Johnston et al. [2] and Palmiotti et al. [11] correlate the creation of "wormlike" defects to previously present shunt-like defects in the device acting as "seeds" for the hotspot propagation.

The formation of local shunts due to partial shading is a fast process. Wendlandt and Podlowski observed permanent performance loss and the creation of shunt-like defects due to a 10 ms light flash of 1000 W/m^2 while shading 10% of the module surface [8]. Silverman et al. furthermore, created permanent shunts in a partial-shade stress test with several 100 ms light pulses (1000 W/m^2) and a 90% opaque mask covering 90% of several adjacent cells [4]. The short time scale of the investigation makes it difficult to study the initial stages of local defect creation in CIGS solar cells under reverse-bias conditions.

Furthermore, the underlying mechanisms are theoretically not well understood. The Zener and avalanche breakdown mechanisms are not consistent with the strong temperature dependence of the breakdown current [14,15]. Therefore, Szaniawski et al. suggest the thermally activated Poole–Frenkel transport mechanism, which alone, however, does not account for the observed light-enhanced reverse breakdown in CIGS [14].

In this paper, we present pulsed reverse-bias experiments to limit the time scale of defect creation. We stress CIGS mini modules with 10 ms reverse-bias pulses of stepwise increased amplitude, while measuring the electrical current and the thermal response by means of a thermography video. Additionally, we investigate the difference in reverse breakdown behavior between encapsulated and unencapsulated cells.

2. Experimental

2.1. Samples and Set-Up

The CIGS mini-modules used in this study were cut from non-encapsulated industrial semi-fabricated CIGS modules with a ZnO/CdS/Cu(In,Ga)Se$_2$/Mo layer stack. The CIGS absorber was prepared by coevaporation [16]. Each CIGS mini-module consists of 16 in-series connected cells with a cell dimension of 8.4×0.4 cm$^2 = 3.36$ cm^2. We sacrificed every third cell to create contacts to sub-modules consisting of two cells in series connection. Figure 1 illustrates a mini-module divided into five sub-modules. The two cells of each sub-module are connected in series with a *P1/P2/P3* scribing line structure. The *P1* scribing line separates the molybdenum back contact while the *P3* scribing line separates the cell structure (ZnO/CdS/Cu(In,Ga)Se$_2$) of two adjacent cells. The *P2* scribing line connects the back and front contact of two adjacent cells with ZnO and therefore establishes the series connection. The top and bottom edges of the mini-modules were produced similarly to the *P3* scribing line with mechanical scribing down to the Mb back contact. Therefore, the top edge, bottom edge, and *P3* have a similar microscopic structure. The experiments are conducted on encapsulated and non-encapsulated (unencapsulated) mini-modules. For the encapsulation process, we employed a conventional ethylene-vinyl acetate (EVA) foil, which is also used in common industrial lamination processes.

Dark current-voltage (I/V) characteristics are measured with a Keithley 2425 100 W source measure unit (SMU) (Keithley Instruments, Inc., Cleveland, OH, USA) between -1.0 V and 1.5 V with a step voltage of 25 mV and a waiting time of 0.1 s. The pulsed reverse stress is applied using a Tektronix AFG 3022B pulse generator (Tektronix UK Ltd., Bracknell, UK). The signal is then amplified by a factor of 5 with a KEPCO bipolar operational power supply/analyzer (KEPCO, Naju-si, Republic of Korea), and measured with an Agilent Technologies DSO 1004A oscilloscope (Agilent Technologies, Inc., Santa Clara, CA, USA). The electrical response (current) is measured with an oscilloscope by measuring the voltage drop across a Vishay RTO 20F 1 Ω thick film resistor (Vishay Intertechnology, Inc., Malvern, PA, USA), connected in series to the sample. The thermal response of the sample is then determined using an IRCAM Velox 327k SM thermography camera (IRCAM GmbH, Erlangen, Germany), which is equipped with an indium antimonide (InSb) detector, sensitive in the spectral range of 1.5 to 5.5 μm with a resolution of 640×512 pixels.

The thermography camera and the pulse generator are connected via a rectangular signal encoder (Agilent Technologies N6700B, Agilent Technologies, Inc., Santa Clara, CA, USA) to establish a fixed temporal relation between measured infrared signal and electrical stimulation (reverse-bias pulse) on the sample. The rectangular signal encoder is triggered by the "IRCAM works" camera software [17].


(**a**)   (**b**)
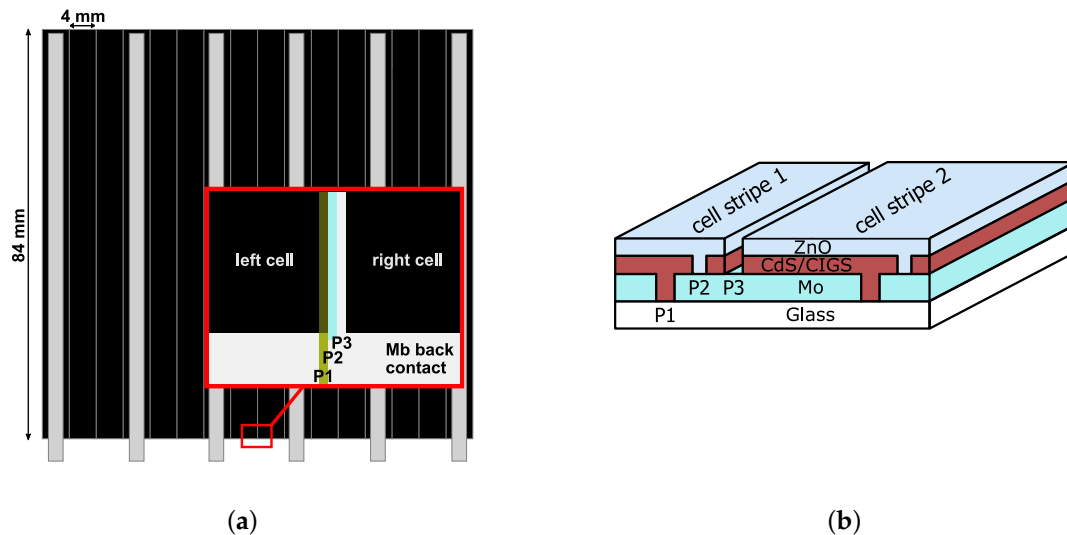
Figure 1. Schematic illustration of (**a**) a mini-module devided into five sub-modules consisting of two series-connected cells with a cell dimension of 8.4×0.4 cm^2 = 3.36 cm^2; (**b**) the *P1/P2/P3* scribing line structure that establishes the series interconnection of two cell stripes. Top and bottom edge of the mini-module are produced with mechanical scribing and have, therefore, a similar microscopic structure as the *P3* scribing line.

2.2. Experiment

In the experiment we study the electrical and thermal response of CIGS sub-modules to rectangular reverse-bias pulses. A sub-module consists of two monolithically series-interconnected CIGS solar cell stripes of 8.4×0.4 cm^2. Hereinafter, we will refer to such a sub-module as a sample. In total we investigated 18 encapsulated samples (#1–#18) and 10 unencapsulated samples (#19–#28). The pulse amplitude with a duration of 10 ms (and a rise-time of 1 ms) is step-wise increased (0.1 V per step), starting with a voltage of -5 V, until a breakdown occurs within the sample. Before and after every reverse-bias pulse, the sample is characterized by an I/V measurement to check for permanent damage. Once a newly created defect is identified, it is investigated with an optical microscope.

For every 10 ms pulse we record the thermal response with a thermographic video. The frame rate of the video is 160 frames per second (one frame per 6.25 ms) and each frame has an integration time of approximately 1 ms. Both the start of the thermographic video recording, and the 10 ms reverse-bias pulse, are triggered by a pulse generator. We observed that there is a delay between the trigger and the recording of the first frame of the video (frame 1). We estimate this delay to be approximately 0.5 ms. For this reason we set the thermographic video to acquire one frame (frame 0) in advance. This way, frame 0 is taken approximately 5.25 ms before the actual reverse-bias pulse and the two subsequent frames are within the 10 ms reverse-bias pulse. That is, frame 1 is taken 1.0 ms and frame 2 is taken 7.25 ms after the start of the reverse pulse. In addition, frame 3 is taken 13.5 ms after the start of the pulse (i.e., frame 3 is taken after the 10 ms reverse-bias pulse). Note that all times are approximate. In Figure 2a,b the temporal relation between pulse and thermography image acquisition is indicated with the gray-colored bars (frame 0, frame 1, frame 2, frame 3).
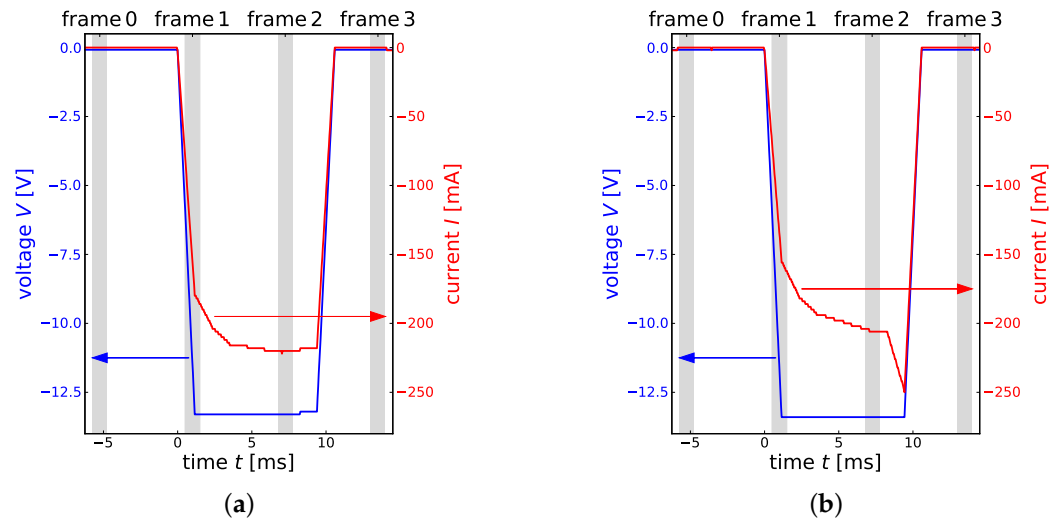
Figure 2. Electrical response of sample #1 to (**a**) a reverse-bias pulse of -13.3 V not causing permanent damage and (**b**) to a reverse-bias pulse of -13.4 V leading to permanent damage. The current surge occurs within the last two milliseconds of the pulse (approximately 8.25 ms after the start of the pulse). The gray-colored bars indicate the times at which the thermography image acquisition of frame 0, frame 1, frame 2 and frame 3 takes place.

3. Results

3.1. Reverse Breakdown Behavior

Figure 2a shows the electrical response of sample #1 to a -13.3 V reverse-bias pulse. This particular pulse did not lead to reverse-bias damage. Contrarily, Figure 2b exemplifies the electrical response of sample #1 to a -13.4 V pulse which did lead to reverse-bias damage. For those pulses which caused permanent damage, we always observe a sudden decrease in current (to a higher negative current level). This current surge may occur anytime during the pulse. In the case of sample #1, the current surge occurs during the last 2 ms of the pulse, as shown in Figure 2b. In other cases, the current surge happened at an earlier time in the pulse, not shown. Furthermore, the sudden surge in current is always accompanied by the appearance of a hotspot in the thermographic video. We did not observe any notable difference in electrical response of encapsulated and non-encapsulated samples.

Figure 3 shows the thermal response associated to the electrical response shown in Figure 2b of frame 1, frame 2, and frame 3. Here, we subtracted the signal of frame 0 from each subsequent frame, such that the signal represents the temperature increase due to the reverse-bias pulse, in relative units. In frame 1, the thermography signal is very low, as not much heat was dissipated in the sample yet. For frame 2, the sample shows a nearly equally distributed temperature rise (in both solar cells) due to the reverse-bias pulse. In frame 3, a hotspot is clearly visible in the lower part of the left solar cell. Note that the current surge occurs in between the acquisition of frame 2 and frame 3 (see Figure 2b) and thus the associated hotspot is only visible in frame 3. Since the camera calibration range is -10 to 50 °C, and the camera is overexposed at the hotspot, the temperature rise within the hotspot must be >30 K above room temperature ($T_{room} \approx 20$ °C). Note that in the case presented, the thermography camera captures the temperature of the encapsulant. Therefore, the temperature rise within the hotspot is expected to be even higher.

In case no reverse-bias damage occurs, for example for sample #1 in response to the -13.3 V pulse, we observe a rather homogeneous heat dissipation within the cells (not shown). A figure is omitted for this case as the temperature rise then resembles the first two frames in Figure 3. Note that for unenencapsulated samples we even observe a more homogeneous temperature rise in the two cells due to the absence of the encapsulant.
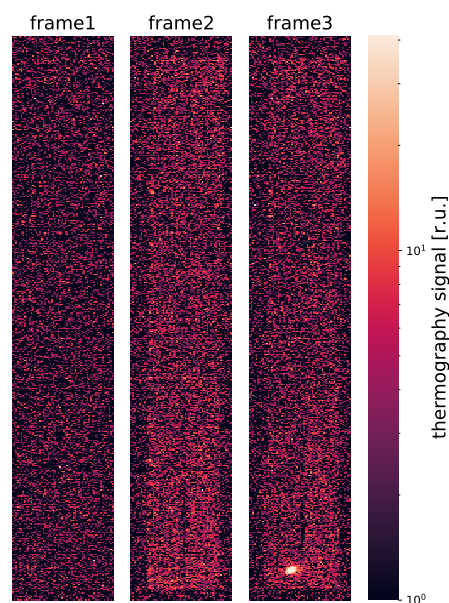
Figure 3. Thermal response of sample #1 to a −13.4 V pulse leading to permanent damage. The thermography signal of the first frame, frame 0, is subtracted from each subsequent frame (i.e., the signal represents the temperature rise due to the reverse-bias pulse. Frames 1, 2, and 3 are rerecorded at approximately 1 ms, 7.25 ms, and 13.5 ms after the start of the pulse, respectively. The thermal response at frame 2 shows a small and fairly homogeneous rise in temperature in both of the two solar cells. A current surge occurs at approximately 8.25 ms after the start of the pulse; see Figure 2b). The associated hotspot is clearly visible in the lower part of the left solar cell in frame 3.

We observe from the dark I/V characteristics before and after pulses, that a current surge during the pulse is always accompanied by a decrease in shunt resistance. Figure 4 exemplifies the visible decrease in shunt resistance for sample #2 before and after an applied −9.0 V pulse. This clearly demonstrates the current surge and appearance of the hotspot in the thermography signal are associated with reverse-bias damage. Furthermore, the results show that a 10 ms of reverse stress is sufficient to create permanent shunt-like defects in CIGS solar cells. Note that the absolute decrease in shunt resistance varies for each sample, but is consistently visible due to the comparison of the I/V characteristics before and after a pulse, showing a current surge.
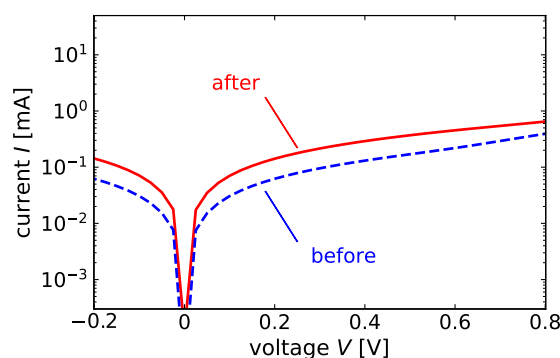
Figure 4. Exemplary comparison of the I/V characteristics of sample #2 before and after a −9.0 V pulse, showing a current surge.

We define the damage threshold voltage as the amplitude of the reverse-bias pulse at which we observe a current surge. The damage threshold voltage statistics show substantial scatter, with damage threshold voltages ranging from −7.5 to −20.6 V. Despite the scatter and small sample size (18 encapsulated and 10 unencapsulated samples), a clear

difference in the susceptibility to reverse stress between encapsulated and unencapsulated solar cells is observed. Figure 5 shows the normalized occurrence of the damage threshold voltage in encapsulated and unencapsulated solar cells. Unencapsulated solar cells are more susceptible to reverse-bias damage, with a mean damage threshold voltage of $V_{\text{mean, unencap}} = 10.2$ V compared to encapsulated solar cells ($V_{\text{mean, encap}} = 14.0$ V).
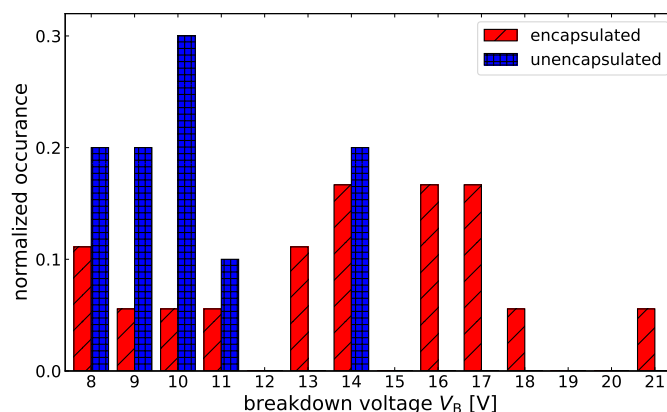
Figure 5. Normalized occurrence of the damage threshold voltage in (18) encapsulated and (10) unencapsulated samples. Despite the small sample size, encapsulated solar cells are found to resist a higher reverse stress than unencapsulated solar cells. Note that the voltages drop over two cells connected in series.

3.2. Post Mortem Analysis

For all samples, we investigated the location where we observed a hotspot under an optical microscope. For all those locations we observe a local change in the CIGS structure, consistent with the creation of a permanent defect. Figure 6a shows an example for a defect created within the solar cell area in the unencapsulated sample #19. The defect area with a diameter of approximately 10 μm exhibits enhanced reflectance with respect to the surrounding CIGS.

For the encapsulated samples, the observation of the CIGS cell under the optical microscope is not possible through the encapsulant. For this reason, we peeled off the encapsulant. However, for some of the samples this led to the removal of the CIGS absorber at the hotspot. If the absorber was removed at the defect site, the stack was completely removed down to the molybdenum back contact. Figure 6b shows the area of a defect (with an approximate diameter of 75 μm) within the solar cell area in sample #3. For this particular sample, the CIGS absorber was removed when the encapsulant was peeled off. The defect site in Figure 6b is as bright as the molybdenum back contact, which is more reflective than the surrounding CIGS. Note, however, that the CIGS absorber was not always removed with the encapsulant. Figure 6c shows an example of a defect where the absorber was not peeled off with the encapsulant.

The defect diameter varies between 10–100 μm. In addition to the point-like (circular) shape, some defects show an elongated shape, which possibly are an early sign of the propagation of the defect through the absorber. Figure 6c shows an example for a defect within the encapsulated sample #4 after removal of the encapsulation. The microscope image shows a defect in the center (indicated with a large red circle) with two protuberances extending downward to the left and upward to the right (indicated by red arrows).

For the unencapsulated samples, in addition to defects such as the defect in Figure 6a, we often observe defects occurring at the top, bottom, and *P3* scribing lines. In fact, the majority of the defects in the unencapsulated samples are created at the solar cell edge, respectively, at *P3*. Figure 7 shows two exemplary defects created at *P3* (a) and the edge (b) in the two unencapsulated samples, #20 and #21, respectively. The defects are marked with red circles. The defect size is comparable to defects within the solar cell area and varies from 10–30 μm. Furthermore, we find a semicircular structure of deposited material on

the molybdenum back contact. This is observed for all investigated defects at the edge, respectively, *P3* in unencapsulated samples.
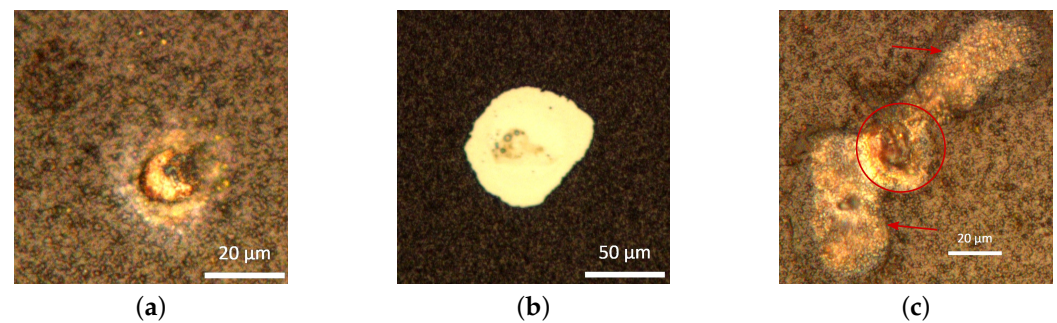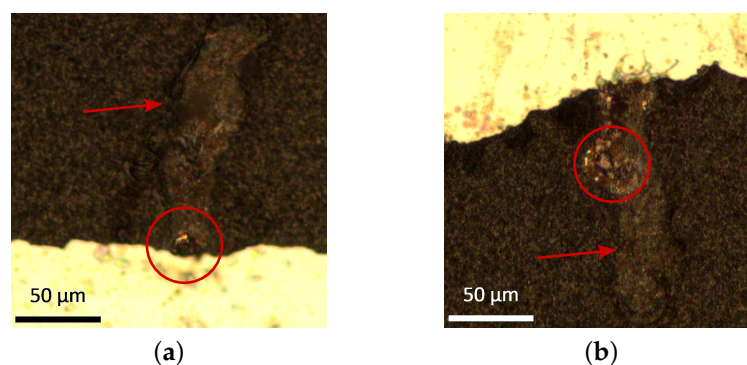

Figure 6. Exemplary images of created defects within the solar cell area. (**a**) Defect within the solar cell area created in the unencapsulated sample #19 visible due to enhanced reflectance, (**b**) defect within the solar cell area (removed solar cell stack in defect area) of the encapsulated sample #3 after removal of encapsulation, visible due to high reflectance of the molybdenum back contact, and (**c**) defect within the solar cell area showing protuberances around the defect for the encapsulated sample #4 after removal of the encapsulation. The big red circle indicates a circular defect in the center of two elongated defect structures, indicated by red arrows.
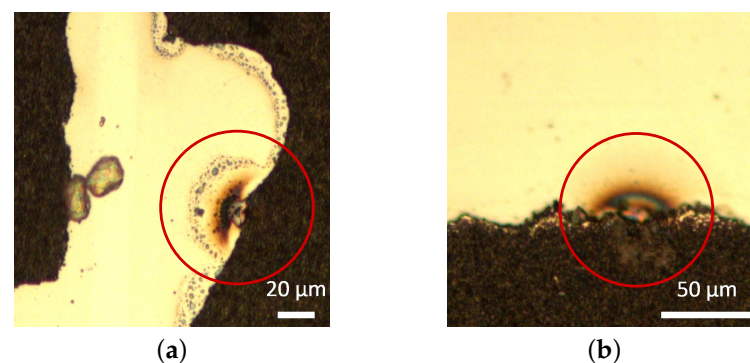
Figure 7. Exemplary images of defects at (**a**) *P3* in the unencapsulated sample #20 and at (**b**) the solar cell edge in the unencapsulated sample #21. The defects are marked with red circles. The defect size of created defects at the edge, respectively, *P3* in the unencapsulated samples varies from 10–30 μm. Around the defect a semicircular structure of deposited material on the molybdenum back contact is visible.

We have not observed this type of edge defect in the encapsulated samples. In encapsulated samples, only a minority of the defects are created at the edge, respectively, in *P3*. Figure 8 shows two exemplary defects at the edge in the encapsulated samples #5 (a) and #6 (b). In contrast to defects at the edge, in unencapsulated samples there is no semicircular structure of deposited material on the molybdenum back contact. Furthermore, the defects are elongated and extend away from the edge into the solar cell interior. In unencapsulated samples, only one defect at the edge shows such an elongated shape.

In some cases, two defects are created within a single pulse. Here we observe that the two defects are never in the same cell. We argue that since the creation of a defect in one of the two cells leads to a reduced shunt resistance of that cell, the voltage drop on the other cell rises abruptly. This in turn greatly increases the probability a second defect is created in the second cell.

(**a**) (**b**)

Figure 8. Microscope images of created defect at the solar cell edge for the encapsulated samples #5 (**a**) and #6 (**b**). The red circle marks the circular defect structure comparable to the defect shown in Figure 6a. The "wormlike" defect structure present in all created defects at edges *P3* in encapsulated samples is indicated by red arrows.

In our experiments, 27 defects were created in encapsulated solar cells and 13 defects are created in unencapsulated solar cells. After the post mortem investigation of the location of defects, we distinguish between three cases:

- Defects *within* the solar cell area;
- Defects at the *edge/P3*;
- Defects at the *P1* line.

The defects at the *P1* line were only observed in unencapsulated examples. The location of the defects are summarized in Table 1.

Table 1. Defect location due to reverse breakdown created defects in encapsulated and unencapsulated solar cells.

Defect Location	Total	*within*	*edge/P3* (**Thereof Elongated**)	*P1*
encapsulated	27	23	4 (4)	0
unencapsulated	13	2	9 (1)	2

Regarding the defect location, we observe a significant difference between encapsulated and unencapsulated samples. While encapsulated solar cells tend to break down within the solar cell area, unencapsulated solar cells tend to break down at the solar cell *edge*, respectively, at the *P3* scribing line.

4. Discussion

A first remarkable result is the timescale in which permanent damage develops in our experiments. For all samples, 10 ms of reverse stress is sufficient to create permanent damage. Furthermore, the experiments show that only a fraction of the pulse duration is necessary to create permanent damage, that is, the duration of the current surge is significantly shorter than the pulse itself. In one case, we found permanent damage after a current surge which started approximately 1 ms before the pulse end. Hence, this defect was created in less than 1 ms. Thereby, the creation of permanent damage develops due to a bias of -13.4 V (approximately -6.7 V on each cell) and therefore at a reverse-bias level, a conventional module could potentially provide during operation at partial-shading conditions. The shortest time scale for the creation of reverse-bias damage in CIGS that we found in the literature was 10 ms [8].

In addition to the creation of permanent local defects, the post mortem analysis reveals that the defects appear to have been locally molten and are often elongated. We consider an indication that the defects here are of the same type as the often reported "wormlike" defects in CIGS cells and modules [9], which also show signs of melt. The reported

"wormlike" defects propagate through the cell under continuous reverse-bias stress. Hence, we believe the observed elongated shape may be a first sign of propagation, starting within the first few ms after the creation of the initial defect. This is in agreement with the work of Johnston et al. and Palmiotti et al. who observed the propagation of hotspots starting at seed defects creating "wormlike" defect structures [2,11].

A second remarkable result is the difference in breakdown behavior in unencapsulated and encapsulated samples. The damage threshold voltage shows a large scatter within the used samples. Nevertheless, encapsulated CIGS solar cells are significantly more resilient to reverse-bias stress (see Figure 5). Furthermore, we find a difference in the location where defects are created. Encapsulated solar cells under reverse stress often break within the cells area, whereas unencapsulated solar cells tend to break at the edges and *P3* line. Thus, the presence of the EVA foil appears to have a large impact on the breakdown behavior.

One possible explanation is arc breakdown. Arc breakdown in air and in a vacuum is most often explained with Paschen's law, depicting a minimum necessary voltage of 340 V.For small gap distances (in the range of less then a μm up to a few μm) however, it has been shown that Paschen's law does not hold and much lower electric fields are necessary [18].The edge and the *P3* scribing line of the CIGS solar cell can both approximately be treated as a 2 μm gap. In our experiments we find breakdown voltages down to 8 V (about 4 V on each solar cell) sufficient to create a defect as shown in Figure 7. Babrauskas provides a detailed overview on the current state of research regarding arc breakdown over small gap distances in air and in a vacuum [18].He states that voltages in the range of 100–200 V are sufficient to trigger a breakdown through air over a gap of 2 μm. Therefore, the observed breakdown voltages seem to be not sufficient (4 V observed, 100–200 V expected to be necessary) for an explanation via arc breakdown. In our experiments however, 4 V on one solar cell might create much higher electric fields than 4 V would create on two perfectly planar electrodes. Due to the production process (mechanical scribing of *P3* and the edge) the edges are rough and the distance between TCO top layer and molybdenum back contact may be locally further reduced. Therefore, field strengths in the range of 50–100 $\frac{V}{\mu m}$ = 50–100 $\frac{MV}{m}$ do not seem to be impossible in the given configuration.

A second possible explanation is the difference in the thermal properties of air in respect to the encapsulant. It is known that the junction breakdown voltage in CIGS solar cells reduces with temperature [14,15]. The higher thermal resistance of air in respect to the EVA foil might enhance the local temperature of the solar cell at the edge in an early stage of defect creation. Therefore, the local current might be increased (or, respectively, the local junction breakdown voltage might be decreased) enhancing the local temperature, closing a positive feedback loop of local current and local temperature and leading to permanent damage.The presence of such a positive (electrothermal) feedback loop in CIGS solar cells under reverse stress was theoretically described by Karpov [19] and Nardone et al. [20]. Recent experimental work [21,22] has further demonstrated that for CIGS under reverse stress the electrothermal feedback loop is a mechanism that can cause the type of defects described here. The difference in heat diffusion due to the absence of the encapsulant at the edge might therefore lead to preferred defect creation at the solar cell edge in unencapsulated CIGS solar cells.

Further, we consider surface flashover at the edges of unecapsulated solar cells. Surface flashover at semiconductor edges can arise at significantly lower voltages then voltages necessary to overcome the expected bulk dielectric strength [23]. Williams and Peterkin attribute band bending at the semiconductor surface and, therefore, an increased surface conductivity as a possible mechanism of surface flashover. Thereby, the theory expects thermally excited carriers to increase the local free carrier density exponentially with temperature. An increased thermal mass at the semiconductor edge is then expected to mediate a resulting electrothermal feedback loop. Therefore, the presence of an EVA foil is expected to suppress surface flashover effects.

5. Summary

In this paper we introduced an experiment where encapsulated and unencapsulated CIGS solar cells are stressed with a short reverse-bias pulse. We show that reverse-bias defect creation in CIGS solar cells is a fast process. The experiments reveal that a short timescale of approximately 1 ms is sufficient to create a permanent defect under reverse-bias conditions that have relevance to PV applications. Furthermore, we show the reverse-bias defect creation in CIGS solar cells is strongly affected by the presence of an encapsulation. Unencapsulated solar cells are much more prone to reverse-bias damage, and tend to break at the edges of the solar cell. We speculate this effect may be due to arc breakdown, the thermal mass of the EVA mediating a positive feedback effect of local temperature and local current or due to flashover effects at the solar cell edge, mediated by the presence of the EVA.

Author Contributions: Conceptualization, B.E.P.; methodology, T.S.V. and B.E.P.; software, T.S.V. and A.G.; validation, T.S.V., B.E.P., A.G. and U.R.; formal analysis, T.S.V. and B.E.P.; investigation, T.S.V.; resources, A.G. and U.R.; data curation, T.S.V. and B.E.P.; writing—original draft preparation, T.S.V.; writing—review and editing, T.S.V., B.E.P., A.G. and U.R.; visualization, T.S.V. and B.E.P.; supervision, B.E.P., A.G. and U.R.; project administration, B.E.P., A.G. and U.R.; funding acquisition, A.G. and U.R.; All authors have read and agreed to the published version of the manuscript.

Conflicts of Interest: The authors declare no conflict of interest.

References

1. Molenbroek, E.; Waddington, D.; Emery, K. Hot spot susceptibility and testing of PV modules. In Proceedings of the IEEE 22nd Photovoltaic Specialists Conference, Las Vegas, NV, USA, 7–11 October 1991; pp. 547–552.
2. Johnston, S.; Sulas, D.; Palmiotti, E.; Gerber, A.; Guthrey, H.; Liu, J.; Mansfield, L.; Silverman, T.J.; Rockett, A.; Al-Jassim, M. Thin-film module reverse-bias breakdown sites identified by thermal imaging. In Proceedings of the IEEE 7th World Conference on Photovoltaic Energy Conversion (A Joint Conference of 45th IEEE PVSC, 28th PVSEC & 34th EU PVSEC), Waikoloa Village, HI, USA, 10–15 June 2018; pp. 1897–1901.
3. Bakker, K.; Weeber, A.; Theelen, M. Reliability implications of partial shading on CIGS photovoltaic devices: A literature review. *J. Mater. Res.* **2019**, *34*, 3977–3987. [CrossRef]
4. Silverman, T.J.; Deceglie, M.G.; Deline, C.; Kurtz, S. Partial shade stress test for thin-film photovoltaic modules. In Proceedings of the SPIE Reliability of Photovoltaic Cells, Modules, Components, and Systems VIII, San Diego, CA, USA, 9–10 August 2015; pp. 112–123.
5. Wendlandt, S.; Berendes, S.; Weber, T.; Berghold, J.; Krauter, S.; Grunow, P. Shadowing investigations on thin film modules. In Proceedings of the 32nd European Photovoltaic Solar Energy Conference and Exhibition, Munich, Germany, 20–24 June 2016.
6. Silverman, T.J.; Mansfield, L.; Repins, I.; Kurtz, S. Damage in monolithic thin-film photovoltaic modules due to partial shade. *IEEE J. Photovolt.* **2016**, *6*, 1333–1338. [CrossRef]
7. Lee, J.E.; Bae, S.; Oh, W.; Park, H.; Kim, S.M.; Lee, D.; Nam, J.; Mo, C.B.; Kim, D.; Yang, J.; et al. Investigation of damage caused by partial shading of CuInxGa(1-x)Se₂ photovoltaic modules with bypass diodes. *Prog. Photovolt. Res. Appl.* **2016**, *24*, 1035–1043. [CrossRef]
8. Wendlandt, S.; Podlowski, L. Influence of near field shadowing on the performance ratio of thin film modules. In Proceedings of the 35th European Photovoltaic Solar Energy Conference and Exhibition, Brussel, Belgium, 24–27 September 2018; pp. 1230–1235.
9. Westin, P.O.; Zimmermann, U.; Stolt, L.; Edoff, M. Reverse bias damage in CIGS modules. In Proceedings of the 24th European Photovoltaic Solar Energy Conference, Hamburg, Germany, 21–25 September 2009; pp. 2967–2970.
10. Johnston, S.; Palmiotti, E.; Gerber, A.; Guthrey, H.; Mansfield, L.; Silverman, T.J.; Al-Jassim, M.; Rockett, A. Identifying reverse-bias breakdown sites in CuInxGa(1-x)Se₂. In Proceedings of the IEEE 44th Photovoltaic Specialist Conference, Washington, DC, USA, 25–30 June 2017; pp. 1400–1404.
11. Palmiotti, E.; Johnston, S.; Gerber, A.; Guthrey, H.; Rockett, A.; Mansfield, L.; Silverman, T.J.; Al-Jassim, M. Identification and analysis of partial shading breakdown sites in CuInxGa(1-x)Se₂ modules. *Sol. Energy* **2018**, *161*, 1–5. [CrossRef]
12. Guthrey, H.; Nardone, M.; Johnston, S.; Liu, J.; Norman, A.; Moseley, J.; Al-Jassim, M. Characterization and modeling of reverse-bias breakdown in Cu(In,Ga)Se₂ photovoltaic devices. *Prog. Photovolt. Res. Appl.* **2019**, *27*, 812–823. [CrossRef]
13. Bakker, K.; Åhman, H.N.; Burgers, T.; Barreau, N.; Weeber, A.; Theelen, M. Propagation mechanism of reverse bias induced defects in Cu(In,Ga)Se₂ solar cells. *Sol. Energy Mater. Sol. Cells* **2020**, *205*, 110249. [CrossRef]

14. Szaniawski, P.; Lindahl, J.; Törndahl, T.; Zimmermann, U.; Edoff, M. Light-enhanced reverse breakdown in Cu(In,Ga)Se$_2$ solar cells. *Thin Solid Film.* **2013**, *535*, 326–330. [CrossRef]

15. Puttnins, S.; Jander, S.; Wehrmann, A.; Benndorf, G.; Stölzel, M.; Müller, A.; Von Wenckstern, H.; Daume, F.; Rahm, A.; Grundmann, M. Breakdown characteristics of flexible Cu(In,Ga)Se$_2$ solar cells. *Sol. Energy Mater. Sol. Cells* **2014**, *120*, 506–511. [CrossRef]

16. Dimmler, B.; Wächter, R. Manufacturing and application of CIS solar modules. *Thin Solid Film.* **2007**, *515*, 5973–5978. [CrossRef]

17. *IRCAM Works*, Version 3.02; Windows; IRCAM GmbH: Bayern, Germany, 2007.

18. Babrauskas, V. Arc breakdown in air over very small gap distances. In Proceedings of the 13th International Fire Science and Engineering Conference, Nr Windsor, UK, 24–26 June 2013; Volume 2, pp. 1489–1498.

19. Karpov, V. Coupled electron–heat transport in nonuniform thin film semiconductor structures. *Phys. Rev. B* **2012**, *86*, 165317. [CrossRef]

20. Nardone, M.; Dahal, S.; Waddle, J. Shading-induced failure in thin-film photovoltaic modules: Electrothermal simulation with nonuniformities. *Sol. Energy* **2016**, *139*, 381–388. [CrossRef]

21. Vaas, T.S.; Pieters, B.E.; Gerber, A.; Rau, U. Thermal Stimulation of Reverse Breakdown in CIGS Solar Cells. *IEEE J. Photovolt.* **2023**. [CrossRef]

22. Nofal, S.; Pieters, B.E.; Hülsbeck, M.; Zahren, C.; Gerber, A.; Rau, U. A direct measure of positive feedback loop-gain due to reverse bias damage in thin-film solar cells using lock-in thermography. *EPJ Photovolt.* **2023**, *14*, 3. [CrossRef]

23. Williams, P.; Peterkin, F. A mechanism for surface flashover of semiconductors. In Proceedings of the 7th Pulsed Power Conference, Monterey, CA, USA, 11–14 June 1989; pp. 890–892. [CrossRef]